PAPER

Check for updates

Solar driven reduction of CO_2 using Pt–Cu/C as a catalyst in a photoelectrochemical cell: experiment and mechanism study

Xiaoxu Xuan, Jun Cheng, [ID] * Xiao Yang, Junhu Zhou and Kefa Cen

Carbon supported nano-metal catalysts are expected to improve CO_2 reduction selectivity and efficiency due to the addition of more active sites and enhancement of electron transport ability. In this study, HKUST-1 was pyrolyzed and decorated with Pt to prepare Pt–Cu/C catalysts. The catalytic effect of the catalysts with different Pt contents in the CO_2 photoeletrochemical reduction reaction (CO_2PRR) were compared. The total carbon atom conversion rate in CO_2PRR experiments using Pt–Cu/C catalysts first increased to a peak when using 1.6 wt% Pt–Cu/C catalyst and then decreased with the increase of Pt content. The 1.6 wt% Pt–Cu/C catalyst showed good hydrogen evolution reaction (HER) inhibiting ability compared with other Pt–Cu/C catalysts. Density functional theory (DFT) calculations were conducted to give an insight into the CO_2PRR mechanism on some possible active sites in Pt–Cu/C catalysts. The result demonstrated that HER was more likely to be inhibited on the Cu/Pt active surface and at the same time CO_2PRR was promoted.

1. Introduction

Photoelectrochemical reduction of CO_2, as an artificial photosynthesis method to solve both the problems of CO_2 emissions and the shortage of clean energy, is attracting increasing attention.[1–4] However, to date, the low activity of CO_2 photoelectrochemical reduction (CO_2PRR) catalysts still remains a big problem.[5,6]

Heterogeneous catalysts have been widely used in various catalytic reactions,[7–9] especially in CO_2 reduction reactions.[10,11] Previous studies demonstrated that the metal–metal interface played an important role in improving the activity and selectivity of the catalysts.[5,12,13] The hybrid structures of the heterogeneous catalysts may lead to the enhancement of surface charge transfer ability, increasing the surface electron density and improving the adsorption of the intermediates at the surface.

Carbon supported metal nanoparticles heterogeneous catalysts are reported to have effectively catalytic ability to reduce CO_2 to various products.[2,14,15] The carbon supported Cu heterogeneous catalysts have been reported to have high catalytic efficiency in CO_2PRR.[6,16] By introducing noble metal to form noble metal–copper interface, the surface charge transfer ability will be enhanced, thus improving CO_2PRR efficiency.

Metal organic frameworks (MOFs), with high surface area, hybrid features and tunable porosity, multi-functionality and good catalytic selectivity, have drawn increasing attention.[2,17,18] The directly pyrolyzing of MOFs enables the easy synthesis of metal embedded in porous carbon catalyst.[19,20]

Herein, HKUST-1 was chosen as the precursor for synthesizing Pt–Cu/C catalyst in this research. A highly-dispersed HKUST-1 was synthesized using the one-pot thermal method. Then, the obtained Pt–Cu/C catalyst was achieved through pyrolyzation of pristine HKUST-1 under N_2 ambient and reduction under H_2 ambient. In order to study the effect of Pt content on the CO_2PRR and find the optimum Pt content, Pt–Cu/C with various Pt contents were employed in the CO_2PRR. Density functional theory (DFT) calculations were also conducted to clarify the mechanism of Pt–Cu/C catalytic effect on CO_2PRR and inhibiting hydrogen evolution reaction.

2. Experiment

2.1 Preparation of and Pt-TNTs anode

2.1.1 Materials and chemicals. $Cu(NO_3)_2 \cdot 3H_2O$, absolute dimethylformamide (DMF), absolute ethanol, ethylene glycol (EG), NH_4F, and analytical pure chloroplatinic acid (H_2PtCl_6) were purchased from Sinopharm Chemical Reagent Co. Ltd (China). 1,3,5-Benzenetricarboxylic acid (98%) was purchased from Aladdin Co. Ltd. Polyvinylpyrrolidone (PVP) was purchased from Sigma Aldrich Co. Ltd. Nafion 117 membrane and Nafion membrane solution were purchased from Shanghai Hesen Co. Ltd. Copper foam (CF, 100 ppi) was purchased from Taili Suzhou Co. Ltd. And 99.89% Ti foil was purchased from Suzhou Shuanghua Co. Ltd.

2.1.2 Synthesis

Synthesis of Pt–Cu/C catalysts with various Pt contents. The pristine HKUST-1 was firstly synthesized based on a typical hydrothermal method. 0.93 g $Cu(NO_3)_2 \cdot 3H_2O$ and 0.4 g PVP were dissolved in 30 mL DMF and ethanol mixture ($V_{DMF} : V_{ethanol} = 1 : 1$). 0.44 g 1,3,5-benzenetricarboxylic acid was

State Key Laboratory of Clean Energy Utilization, Zhejiang University, Hangzhou 310027, China. E-mail: juncheng@zju.edu.cn

dissolved in 30 mL DMF and ethanol mixture. Then the two as prepared mixtures were stirred for 10 min respectively, after which, the two mixtures were mixed together and stirred for another 30 min. The obtained mixture was then poured into a 200 mL Teflon-lined autoclave and kept under the temperature of 120 °C for 4 h. The obtained blue precipitate was washed by ethanol for several times to remove the extra reagents in the solution and then put into an 80 °C vacuum oven.

After drying for 24 h, the pristine HKUST-1 was put into a tube furnace and heated to 500 °C with a temperature rising rate of 5 °C min^{-1} under N_2 atmosphere. The catalyst was kept under 500 °C for 3 h. HKUST-1 was pyrolyzed during the process and then the Cu/C catalyst was obtained.

Four Cu/C catalyst samples with the weight of 200 mg were then mixed with 20 mL of 0.1 g L^{-1}, 0.2 g L^{-1}, 0.3 g L^{-1} and 0.4 g L^{-1} H_2PtCl_6 solutions respectively. The four mixed solutions were put into an 80 °C drying oven for 2 h. In order to reduce Pt^{4+} to platinum, the dried catalysts were put into the tube furnace and heated to 350 °C with a temperature rising rate of 5 °C min^{-1} under H_2 atmosphere and then kept under 350 °C for 2 h. The obtained catalysts were then marked as 1.2 wt% Pt–Cu/C, 1.6 wt% Pt–Cu/C, 1.8 wt% Pt–Cu/C and 2.3 wt% Pt–Cu/C according to the elemental mapping result.

Fabrication of Pt–Cu/C@CF cathode. 1.5 cm × 3 cm CF was used as cathode base. 45 mg of the four as prepared Pt–Cu/C catalysts were mixed with Nafion membrane solution and deionized water to prepare the inks. Then, the as prepared inks were brushed onto CF by using the drop-dry method.

Pt-TNTs (Pt-titanium nanotubes) anode. Pt-TNTs were synthesized follow the anode oxidation method. The residues on the surface of titanium foil were removed by ultrasonic before the oxidation-process. Then, the titanium foil was oxidized in the fluorine-containing ethylene glycol electrolyte (EG + 0.3% NH_4F + 2 vol% H_2O) for 3 h. The oxidized foil was washed with ethanol to remove extra reagents and placed into the muffle furnace to be calcined under the temperature of 450 °C for 3 h.

The TiO_2 nanotubes will be turned into anatase after the calcination process. The obtained anatase TiO_2 nanotubes on the titanium sheet was then deposited with Pt nanoparticles in H_2PtCl_6 solution (depositing current density: 2.5 mA cm^{-2}) to improve its photocatalytic performance.

2.2 Characterization methods

X-ray diffraction (XRD) analysis was performed using an X'Pert PRO (PANalytical, Netherlands) diffractometer with Cu-Kα radiation. The morphology of Pt–Cu/C catalysts were characterized by field-emission scanning electron microscopy (FESEM) using SU-8010 (Hitachi, Japan) and Transmission Electron Microscope (TEM) using JEM-2100. Elemental mapping was conducted on the FESEM system equipped with an energy-dispersive X-ray (EDX) analytical system. The X-ray spectroscopy (XPS) analysis was conducted using a VG ESCA-LAB MARK II X-ray photoelectron spectrometer equipped with Mg-Kα radiation. Brunauer–Emmett–Teller (BET) analysis was conducted to measure the specific surface area of the catalyst

on a Micromeritics ASAP 2020. Electrochemical characterizations were conducted on Ivium-4-stat electrochemical workstation.

2.3 CO_2 photoelectrochemical reduction in PEC

An H-shaped double chamber reaction cell was used to perform the CO_2 photoelectrochemical reduction reaction. The two chambers was separated by a Nafion 117 membrane. Light was applied to anode Pt-TNTs to generate light current and 2 V voltage was applied between the anode and cathode during the reaction. The photocurrent was detected with Ivium-State electrochemical workstation, and sunlight was simulated using Perfectlight PLS-SXE300CUV xenon lamp.

The anolyte was 0.5 M H_2SO_4, while the catholyte was 0.5 M $NaHCO_3$ solution. The liquid and gas products were detected with Agilent GC7820A gas chromatography, while the acids in the liquid products were detected with Dionex Integrion HPIC.

2.4 Theoretical calculation method

DFT calculations in this research were performed using the plane-wave pseudopotential code Vienna Ab initio Simulation Package. The energy cut off of the system was set to 400 eV. The Brillouin zones of all the surfaces were sampled with a 3 × 3 × 1 gamma grid in optimization calculations. The self-consistent electronic convergence limit was set to 1 × 10^{-5} eV.

Two models contain 4 layers of Pt (111) and in-plane periodicity of (3 × 3) Cu layer or CuO layer and a 4 × 4 × 4 Pt (111) periodic surface model are built for representing Cu/Pt, CuO/Pt interfaces and Pt surface respectively according to the characterization results.

3. Results and discussions

3.1 Characterizations of Pt–Cu/C catalysts with various Pt contents

XRD patterns of the Pt–Cu/C catalysts with various Pt contents were shown in Fig. 1(a). In Fig. 1(a), XRD patterns exhibited strong diffraction peaks at 43.3°, 50.4° and 74.2°, indicating the existence of Cu crystal in Pt–Cu/C catalyst. The magnified main characteristic peak of Cu [Fig. 1(b)] showed gradual sharpness of the peaks as the content of Pt decreased, indicating the decrease of crystal size of Cu particles as the Pt content increased. And the Cu particles in the four catalysts were calculated to be ~110 nm, ~100 nm, ~80 nm and ~60 nm respectively. Also, the characteristic peak showed slight shift to lower angle as the Pt content increased, this was due to the reason that the added Pt was alloyed with Cu nanoparticles, and the feature may be benefit to prevent Cu nanoparticles from alloying together.

Diffraction peaks at 32.5°, 35.5°, 36.5°, 48.8°, 53.4°, 58.1°, 61.5°, 66.3° and 67.9° were also observed, and these peaks were corresponded to copper oxide and cuprous oxide.[16,21,22] The diffraction peaks at 42.2° and 72.1° indicated the existence of Pt particles in the catalysts.

SEM micrographs of pristine HKUST-1 and Pt–Cu/C catalysts were exposed in Fig. 2. Accordingly, HKUST-1 [Fig. 2(a) and (b)]
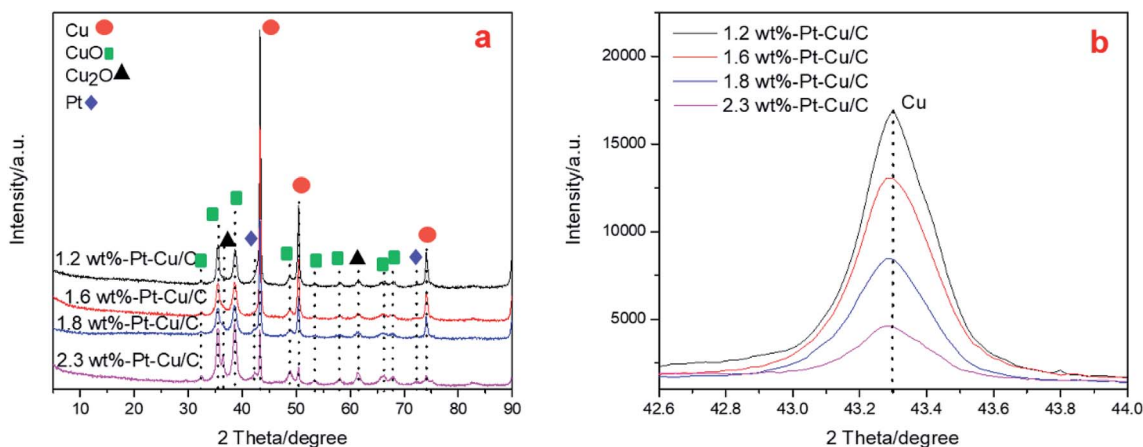
Fig. 1   XRD patterns of 1.2 wt% Pt−Cu/C catalyst, 1.6 wt% Pt−Cu/C catalyst, 1.8 wt% Pt−Cu/C catalyst and 2.3 wt% Pt−Cu/C catalyst (a), magnified Cu characteristic peaks of the four catalysts (b).
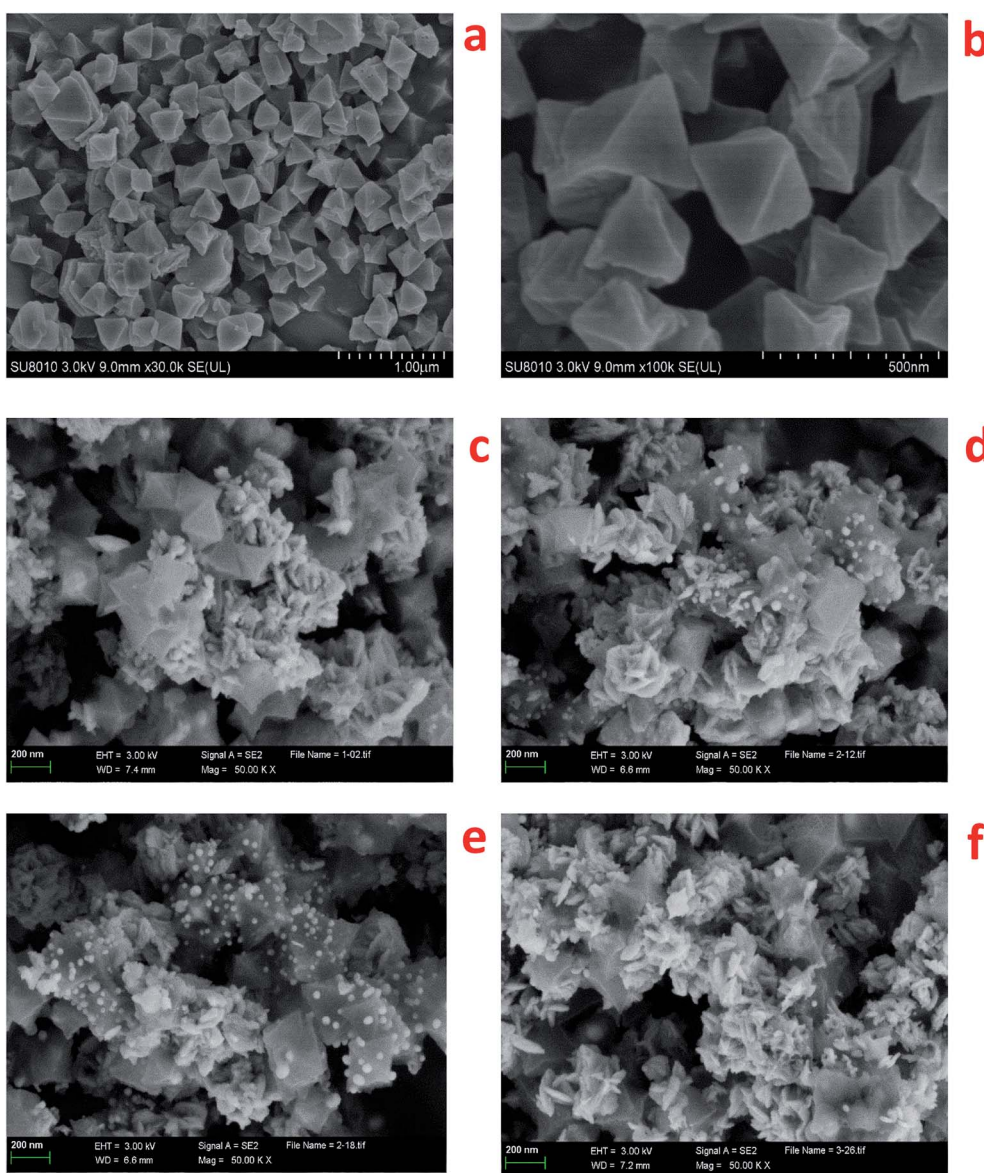

Fig. 2   SEM micrographs of HKUST-1: ×30k (a), ×100k (b); Pt−Cu/C catalysts ×50k: 1.2 wt% Pt−Cu/C (c), 1.6 wt% Pt−Cu/C (d), 1.8 wt% Pt−Cu/C (e) and 2.3 wt% Pt−Cu/C (f).

Table 1 The elemental mapping result of the four catalysts

Element	1.2 wt% Pt–Cu/C (wt%)	1.6 wt% Pt–Cu/C (wt%)	1.8 wt% Pt–Cu/C (wt%)	2.3 wt% Pt–Cu/C (wt%)
C	40.2	43.33	35.21	25.04
O	16.74	12.21	10.22	7.78
Cu	41.86	42.83	52.73	64.93
Pt	1.2	1.63	1.84	2.25

with octahedral shape was successfully synthesized, and Pt–Cu/C catalysts showed similar octahedral shape except that the surface of Pt–Cu/C catalyst was covered by nanoflakes. As the Pt content increased, more nanoflakes were observed on the surface. Elemental mapping was also conducted to evaluate the content of each element in the Pt–Cu/C catalysts. As shown in Table 1, the catalysts mainly contained four kinds of elements including Cu, Pt, C and O. The ratio of Pt atoms *versus* Cu atoms reached topmost of 0.0125 in 1.6 wt% Pt–Cu/C catalyst, indicating higher chance of Pt and Cu binding together in 1.6 wt% Pt–Cu/C catalyst compared with other Pt–Cu/C catalysts.

To clarify the inner structure of the Pt–Cu/C catalysts, TEM characterization was conducted. According to Fig. 3, many nanopores were observed on the carbon base, indicating the porous property of the catalysts. Besides, many solid nanoparticles were embedded inside the Pt–Cu/C catalysts. And the nanoparticles in 1.2 wt% Pt–Cu/C, 1.6 wt% Pt–Cu/C, 1.8 wt% Pt–Cu/C were measured to be 150 nm, 90 nm, 70 nm respectively, which were corresponded to the XRD results, indicating that these solid nanoparticles were Cu nanoparticles. As many nanoflakes covered the surface of 2.3 wt% Pt–Cu/C catalyst, the nanoparticles inside the catalyst were difficult to be observed. As more nanoflakes appeared with the increase of Pt content, they would block the nanopores which lead to much lower mass transfer rate and reaction efficiency. To confirm the suspension, N_2 sorption isotherms of the four catalysts were measured (Fig. 4). Accordingly, the BET surface area decreased from 94.1 m^2 g^{-1} to 80.8 m^2 g^{-1} as Pt content increased, which was in good agreement with the TEM characterization result.

Elemental mapping (Fig. 5) was conducted to clarify the chemical compositions of the Pt–Cu/C catalyst. Accordingly,
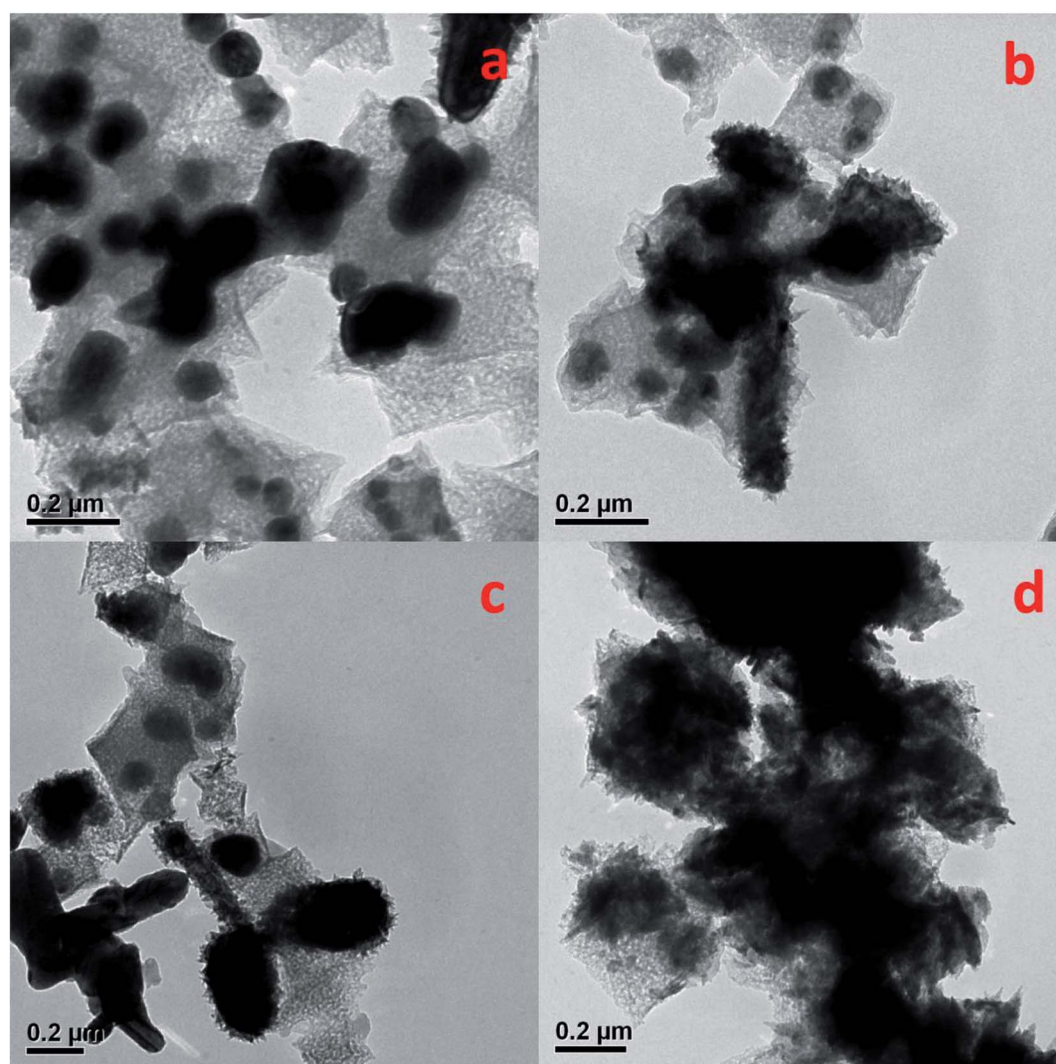

Fig. 3 TEM micrographs of 1.2 wt% Pt–Cu/C (a), 1.6 wt% Pt–Cu/C (b), 1.8 wt% Pt–Cu/C (c) and 2.3 wt% Pt–Cu/C (d).
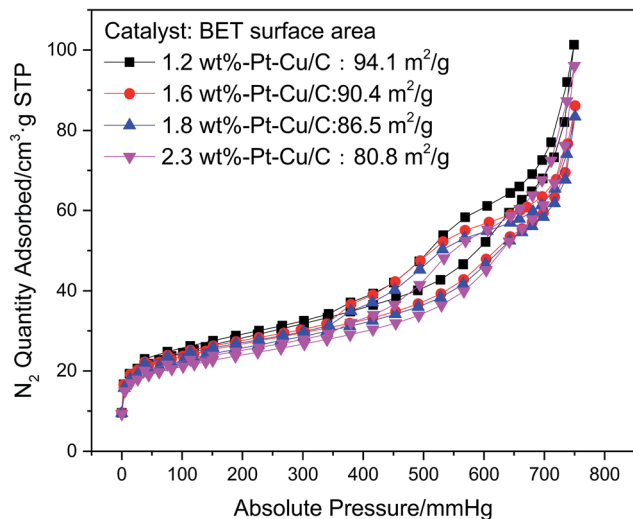
Fig. 4 N$_2$ sorption isotherms of the four Pt–Cu/C catalysts with various Pt contents.

carbon formed the base of the catalyst with Cu nanoparticles inside the carbon matrix. Pt nanoflakes covered the surface of the catalyst. And oxygen could only be observed on partial area, which overlapped with the Cu area, indicating that these particles were Cu$_x$O. The presence of these oxides may be due to the reason that Cu nanoparticles were not stable and could easily be oxidized in the air.

XPS measurement was performed to clarify the valence states and contents of the elements in Pt–Cu/C catalysts. C 1 s spectra

of the four catalysts with various Pt contents were shown in Fig. 6. The XPS spectra were assigned to the corresponding species through a deconvolution fitting procedure. C1s XPS spectra for all the four catalysts were fitted into four components, located at around 281, 282, 283 and 285 eV, corresponding to C–Metal (C–M), C–C, C–O and C=O respectively. And according to the fitting result, 1.6 wt% Pt–Cu/C catalyst possessed the largest content of C–C (46.5% of the C element), which indicated better charge transfer ability.

Cu 2p XPS spectra (Fig. 7) showed typical Cu 2p$_{1/2}$ and Cu 2p$_{3/2}$ peaks in all the four catalysts. The Cu 2p XPS spectrum of 1.2 wt% Pt–Cu/C [Fig. 7(a)] was fitted into two components, and the species with lower bonding energies (BE) was corresponded to Cu^0, the other was assigned to Cu^{2+}. With the increase of Pt content, Cu^{2+} satellite peaked at higher binding energy, indicating the increased content of Cu^{2+} species in 1.6 wt% Pt–Cu/C, 1.8 wt% Pt–Cu/C and 2.3 wt% Pt–Cu/C. Moreover, as the content of Pt increased, the peaks shifted to lower binding energies, indicating the increase of Cu–Pt bonds.

The XPS spectra of the Pt 4f region are presented in Fig. 8. All the Pt–Cu/C catalysts curves were fitted to two peaks, indicating the existence of Pt nanoparticles in the reduced state. The binding energy of Pt 4f shifted to higher binding energy as the content of Pt increased, suggesting the stronger binding of Pt with Cu in the catalysts with higher Pt content.

3.2 CO$_2$ photoelectrochemical reduction

The performance of Pt-Cu/C catalysts in CO$_2$PRR was tested by employing the catalyst in a photoelectrochemical reduction cell
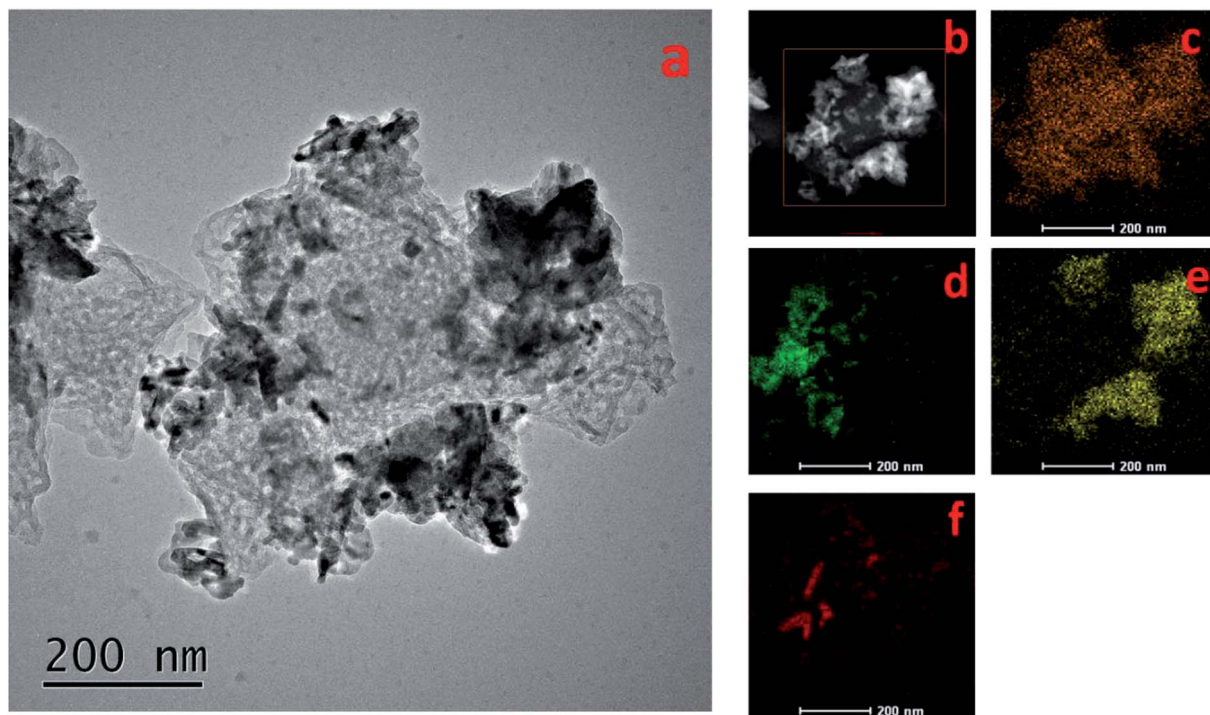

Fig. 5 Elemental mapping of the Pt–Cu/C catalyst, TEM pattern (a), HAADF pattern of the Pt–Cu/C catalyst (b); C elemental mapping (c), Cu elemental mapping (d), Pt elemental mapping (e) and O elemental mapping of the selected area on the Pt–Cu/C catalyst (f).
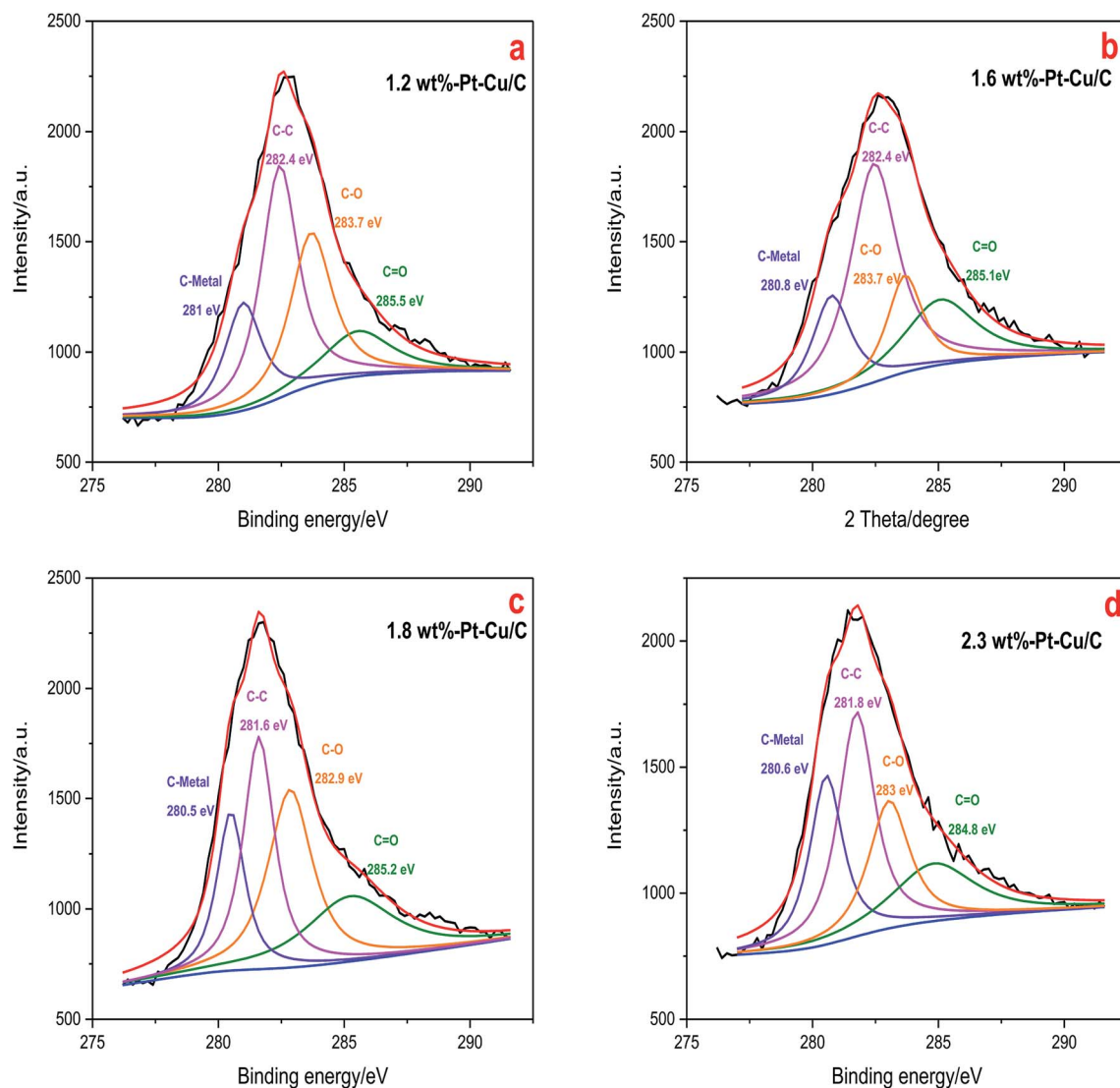
Fig. 6 C 1 s XPS spectra of 1.2 wt% Pt−Cu/C catalyst (a), 1.6 wt% Pt−Cu/C catalyst (b), 1.8 wt% Pt−Cu/C catalyst (c), 2.3 wt% Pt−Cu/C catalyst (d).

(PEC). And the catalysts with various Pt contents were used to figure out the optimum Pt content of the catalyst in promoting CO_2PRR efficiency. Control experiment with N_2 purged using 1.6 wt% Pt−Cu/C as catalyst was also conducted to confirm that the products were all produced from CO_2 reduction, the result showed that only H_2 can be detected in the gas phase products and the H_2 generation rate was 7.32 μmol h^{-1} cm^{-2}, no liquid product was detected. The experimental results of CORPRR were shown in Fig. 9.

The carbon atom conversion rate was calculated using the following equation,

$$\text{Carbon atom conversion rate} = \frac{M_p \times n_p}{t \times A} \quad (1)$$

In which M_p is the molar amount of the product, n_p is the number of carbon atom in the product molecular, t is the reaction time and A is the area of the cathode.

Accordingly, 1.6 wt% Pt−Cu/C catalyst showed the best catalytic effect to reduce CO_2 as the total carbon atom conversion rate reached 1139 nmol h^{-1} cm^{-2}. Liquid products selectivity towards high-order organics including ethanol and propanol was high at first. However, when 2.3 wt% Pt−Cu/C was employed in the PEC system, more C1 organic (e.g. methanol) was generated.

The H_2 generation rate increased from 2.17 μmol h^{-1} cm^{-2} to 10.98 μmol h^{-1} cm^{-2} with the increase of Pt content. Obviously, 1.6 wt% Pt−Cu/C showed the best catalytic activity as it had the highest total carbon atom conversion rate and a relatively low H_2 generation rate.

Light and dark current densities of the PEC system using the four Pt-Cu/C catalysts with various Pt contents were shown in Fig. 10(a). It was demonstrated that the light current of the system was much higher than the dark current, indicating the compensation of light energy to the system in a CO_2 photoelectrochemical reduction reaction cell. And the light current
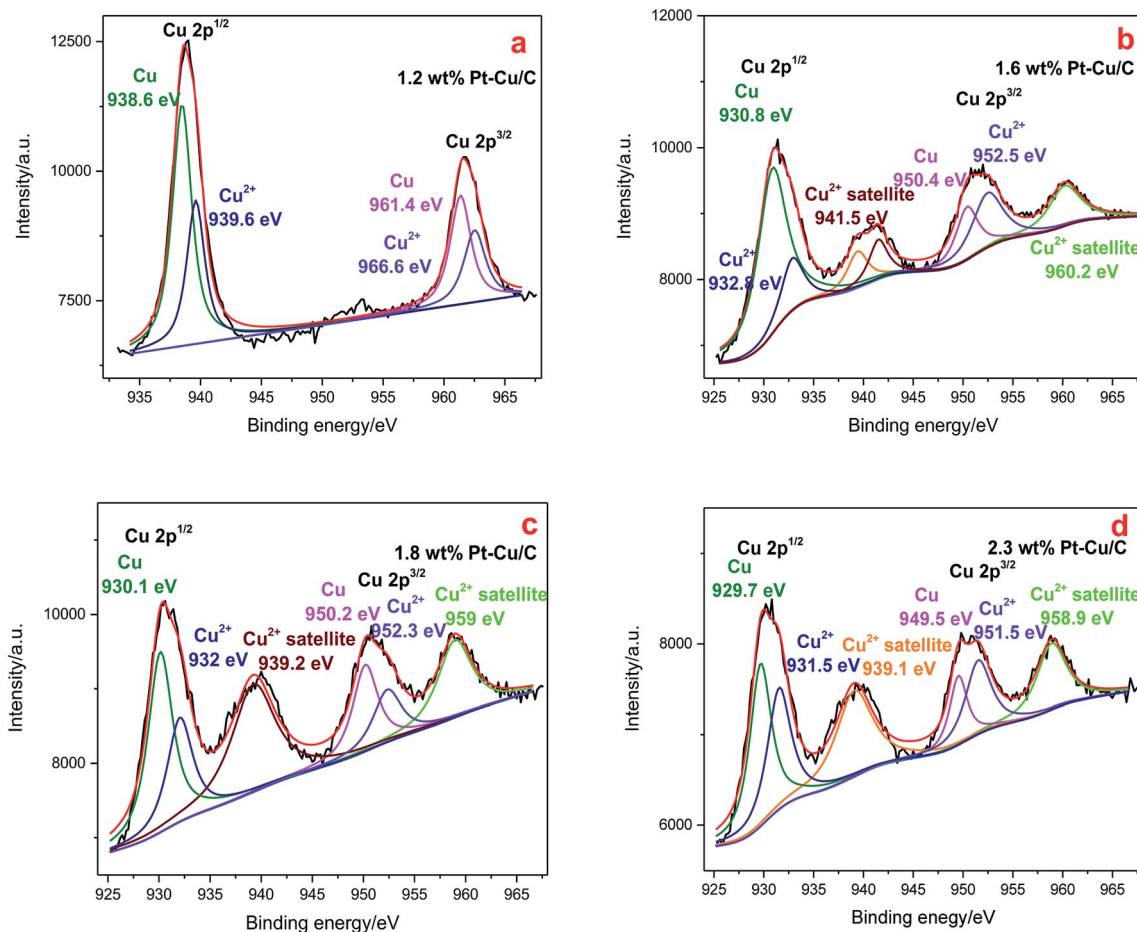
Fig. 7 Cu 2p XPS spectra of 1.2 wt% Pt–Cu/C catalyst (a), 1.6 wt% Pt–Cu/C catalyst (b), 1.8 wt% Pt–Cu/C catalyst (c), 2.3 wt% Pt–Cu/C catalyst (d).

densities of the system when using 1.2 wt% Pt–Cu/C, 1.6 wt% Pt–Cu/C, 1.8 wt% Pt–Cu/C and 2.3 wt% Pt–Cu/C were 3.4 mA cm^{-2}, 3.1 mA cm^{-2}, 2.8 mA cm^{-2} and 2.6 mA cm^{-2} respectively. The adding of Pt to the catalysts would improve the electrochemical performance.

Stability of the Pt–Cu/C catalyst [Fig. 10(b)] was also examined. As all the four catalysts had similar morphology and compositions, the stability test was conducted by using the 1.6 wt% Pt–Cu/C catalyst which had the highest catalytic activity during the CO_2PRR. Accordingly, after 20 CV circles in $NaHCO_3$ solution in a three electrode cell, an RSD of 3.61% was acquired. Indicating good stability of the catalyst.

3.2.1 DFT calculations. According to previous studies,[3,23] metal–metal surface always played an important role in CO_2 reduction reactions. In conjunction with the XRD, XPS and element results discussed above, the theoretical models of Cu/Pt, CuO/Pt surfaces and Pt surface were built to understand the microscopic mechanism of CO_2PRR on the catalyst surface.

CO was an important intermediate in CO_2 reduction to various organics,[24] to study the competition reactions of CO_2PRR and H_2 evolution on different surfaces, the free energy pathways of CO generation and H_2 generation were compared [Fig. 11]. By comparing the free energies of the CO forming

reaction and the H_2 evolution reaction, it was clear that the step of $2H^* \rightarrow {}^*H_2$ on Cu/Pt surface experienced an energy ascending process, and the free energy difference (2.7 eV) was the largest, indicating that H_2 evolution reaction was strongly inhibited on Cu/Pt surface. Besides, Cu/Pt surface also showed best absorbed CO species selectivity as the free energy of the step of ${}^*COOH + H^+ \rightarrow {}^*CO + H_2O$ dropped sharply. Moreover, the binding energies of CO on Cu/Pt surface, CuO/Pt surface and Pt surface were calculated to be −1.05 eV, −0.47 eV and 0.73 eV respectively. Indicating the strongest bonding of CO on Cu/Pt surface, the adsorbed CO species on the catalyst surface then would take part in further C–C bonding reactions to form high-order organics.[24,25] Herein, Cu/Pt surface was calculated to have the best catalytic activity in CO_2PRR and at the same time inhibited hydrogen evolution. In conjunction with the CO_2PRR experimental results and the elemental mapping result, it was supposed that the 1.6 wt% Pt–Cu/C catalyst had more Cu/Pt surface exposed compared to other catalysts. The reason why the CO_2PRR carbon atom conversion rate first increased to a peak at 1.6 wt% Pt–Cu/C and then decreased as the Pt content kept increasing was that the adding of Pt lead to the formation of Cu/Pt surface at first and with the content of Cu/Pt surface increased, the absorbed CO species selectivity was improve and
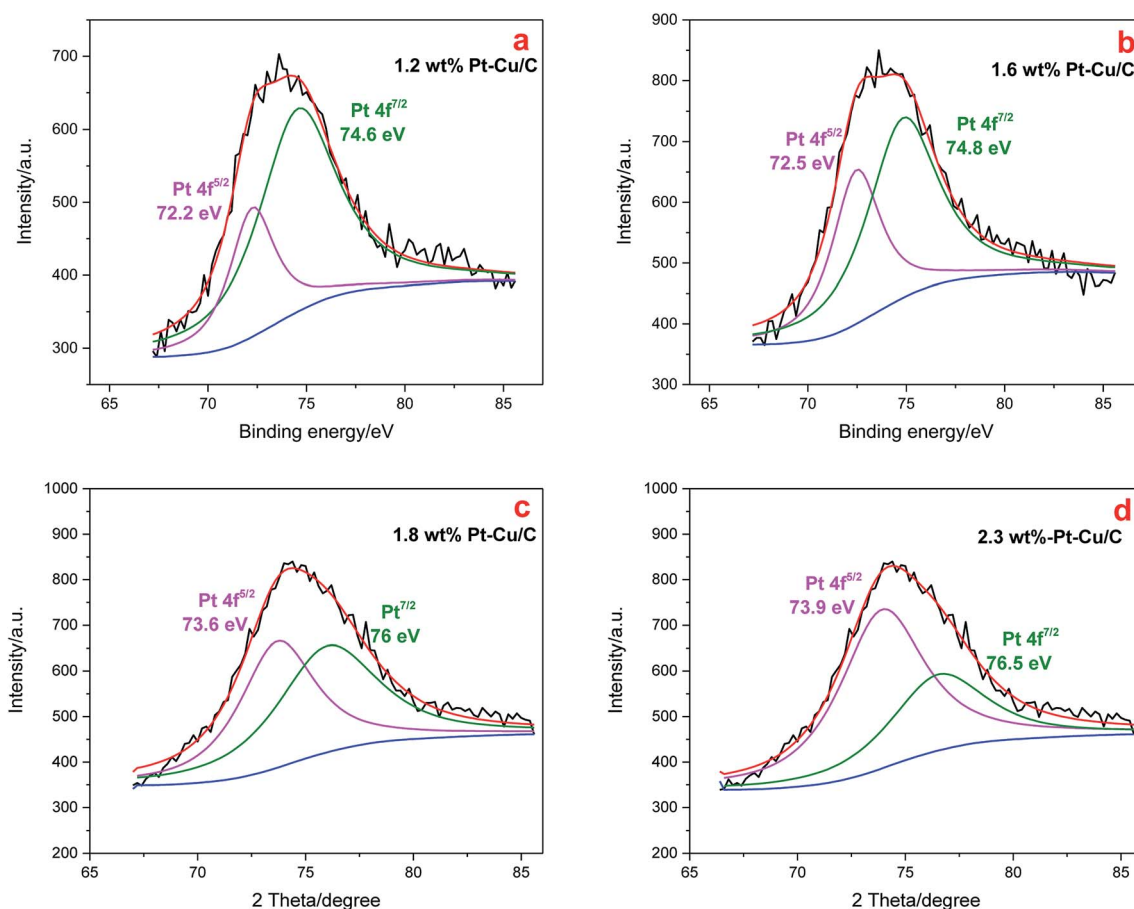
Fig. 8 Pt 4f XPS spectra of 1.2 wt% Pt−Cu/C catalyst (a), 1.6 wt% Pt−Cu/C catalyst (b), 1.8 wt% Pt−Cu/C catalyst (c), 2.3 wt% Pt−Cu/C catalyst (d).
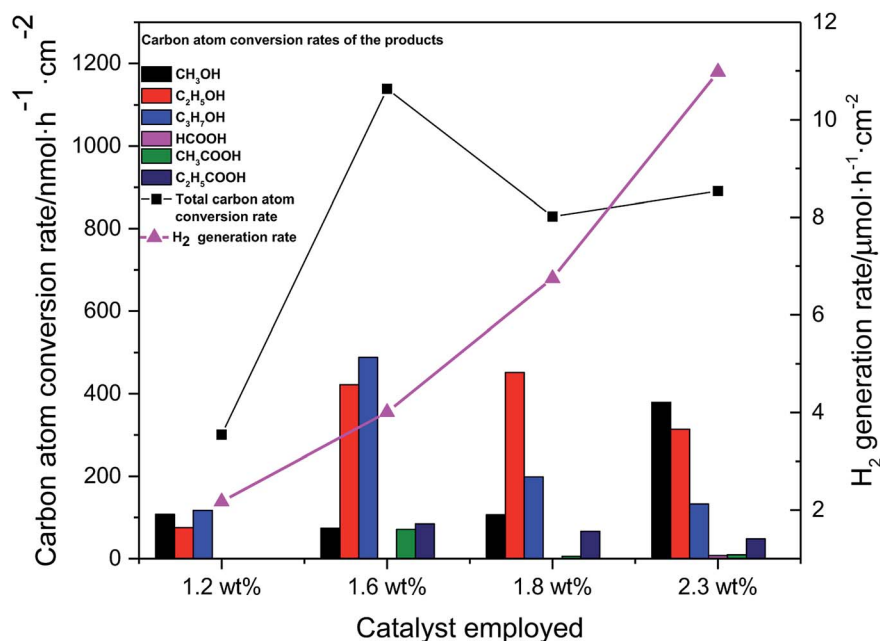

Fig. 9 Carbon conversion rates and H_2 generation rate of CO_2 photoelectrochemical reduction reaction on four catalysts (1.2 wt% Pt−Cu/C catalyst, 1.6 wt% Pt−Cu/C catalyst, 1.8 wt% Pt−Cu/C catalyst, 2.3 wt% Pt−Cu/C catalyst).
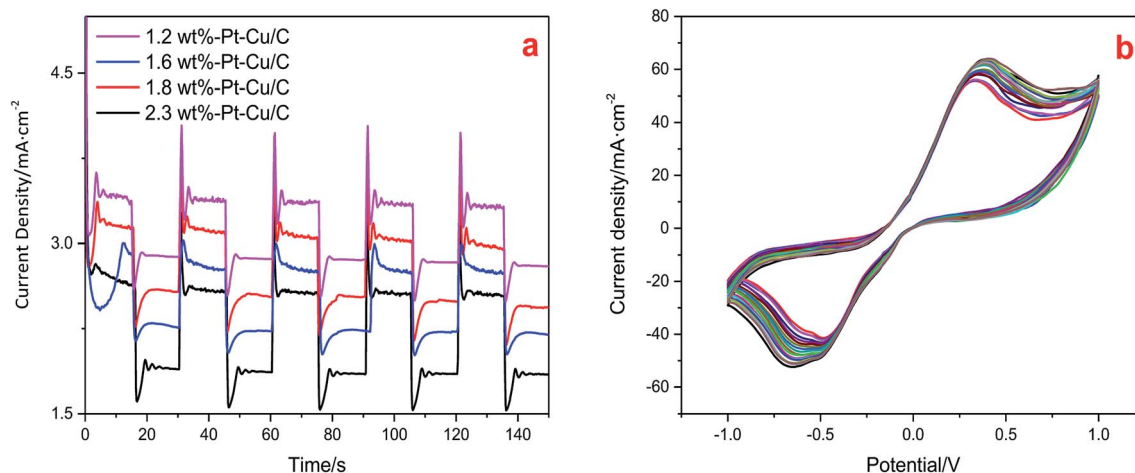
Fig. 10 Light and dark current densities of CO_2 photoelectrochemical reduction system with four catalysts (1.2 wt% Pt–Cu/C catalyst, 1.6 wt% Pt–Cu/C catalyst, 1.8 wt% Pt–Cu/C catalyst, 2.3 wt% Pt–Cu/C catalyst) (a), stability test with 1.6 wt% Pt–Cu/C catalyst (b).
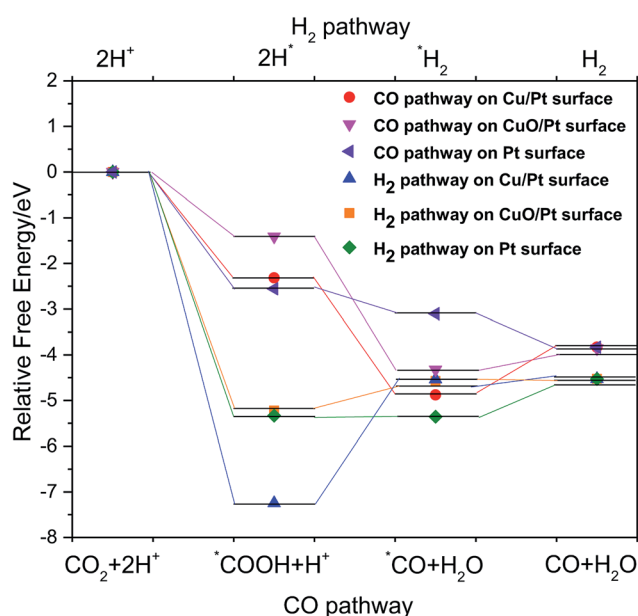

Fig. 11 Relative free energy pathways of producing CO and H_2 on Cu/Pt surface, CuO/Pt surface and Pt surface.

experiments using Pt–Cu/C catalysts first increased to a peak of 1139 nmol h^{-1} cm^{-2} when using 1.6 wt% Pt–Cu/C catalyst and then decreased with the increase of Pt content. The mechanism of Pt–Cu/C catalysts on promoting CO_2PRR was then studied through density functional theory (DFT) calculations. It was demonstrated that Cu/Pt surface had the highest absorbed CO species selectivity and lowest selectivity towards producing H_2. In conjunction with the CO_2PRR experimental results and the elemental mapping result, we could draw the conclusion that the 1.6 wt% Pt–Cu/C catalyst had more Cu/Pt surface exposed compared to other catalysts, the high content of Cu/Pt surface lead to the high activity for CO_2PRR. But for 1.8 wt% Pt–Cu/C and 2.3 wt% Pt–Cu/C, as the Pt content increased, more surface of the catalyst was covered by Pt rather than Cu/Pt surface, resulting in the low organics production and high H_2 generation rate.

Conflicts of interest

There are no conflicts to declare.

Acknowledgements

References

1 S. Aoi, K. Mase, K. Ohkubo, T. Suenobu and S. Fukuzumi, *ACS Energy Lett.*, 2017, **2**, 532–536.
2 J. C. Cardoso, S. Stulp, J. F. de Brito, J. B. S. Flor, R. C. G. Frem and M. V. B. Zanoni, *Appl. Catal., B*, 2018, **225**, 563–573.
3 H. Cho, W. D. Kim, K. Lee, S. Lee, G.-S. Kang, H.-L. Joh and D. C. Lee, *Appl. Surf. Sci.*, 2018, **429**, 2–8.
4 J. F. de Brito, A. R. Araujo, K. Rajeshwar and M. V. B. Zanoni, *Chem. Eng. J.*, 2015, **264**, 302–309.

H_2 evolution reaction was inhibited. However, with the Pt content kept increasing, the surface of the catalyst was covered by Pt rather than Cu/Pt surface, the H_2 evolution reaction was then promoted and less absorbed CO species were produced, resulting in lower organics production.

4. Conclusions

In summary, HKUST-1 was pyrolyzed and decorated with Pt to fabricate Pt–Cu/C catalysts. The as prepared catalysts with various Pt contents were then employed in CO_2PRR and their catalytic activity were compared. The experiment result showed that 1.6 wt% Pt–Cu/C catalyst had the best catalytic activity in CO_2PRR. The total carbon atom conversion rate in CO_2PRR

5 J. Ran, M. Jaroniec and S.-Z. Qiao, *Adv. Mater.*, 2018, **30**, 1704649.

6 D. Raciti and C. Wang, *ACS Energy Lett.*, 2018, **3**, 1545–1556.

7 S. Gong, Z. Jiang, P. Shi, J. Fan, Q. Xu and Y. Min, *Appl. Catal., B*, 2018, **238**, 318–327.

8 T. Wu, Y. Ma, Z. Qu, J. Fan, Q. Li, P. Shi, Q. Xu and Y. Min, *ACS Appl. Mater. Interfaces*, 2019, **11**, 5136–5145.

9 T. Wu, J. Fan, Q. Li, P. Shi, Q. Xu and Y. Min, *Adv. Energy Mater.*, 2018, **8**, 1701799.

10 Y. Wang, S. L. Marquard, D. Wang, C. Dares and T. J. Meyer, *ACS Energy Lett.*, 2017, **2**, 1395–1399.

11 T. Ma, Q. Fan, H. Tao, Z. Han, M. Jia, Y. Gao, W. Ma and Z. Sun, *Nanotechnology*, 2017, **28**, 472001.

12 X. G. Meng, L. Q. Liu, S. X. Ouyang, H. Xu, D. F. Wang, N. Q. Zhao and J. H. Ye, *Adv. Mater.*, 2016, **28**, 6781–6803.

13 N. Rui, Z. Wang, K. Sun, J. Ye, Q. Ge and C.-j. Liu, *Appl. Catal., B*, 2017, **218**, 488–497.

14 E. Pipelzadeh, V. Rudolph, G. Hanson, C. Noble and L. Wang, *Appl. Catal., B*, 2017, **218**, 672–678.

15 L. Wang, Y. Wang, Y. Cheng, Z. Liu, Q. Guo, H. Minh Ngoc and Z. Zhao, *J. Mater. Chem. A*, 2016, **4**, 5314–5322.

16 K. Zhao, Y. Liu, X. Quan, S. Chen and H. Yu, *ACS Appl. Mater. Interfaces*, 2017, **9**, 5302–5311.

17 S. Liu, F. Chen, S. Li, X. Peng and Y. Xiong, *Appl. Catal., B*, 2017, **211**, 1–10.

18 L. Ye, Y. Gao, S. Cao, H. Chen, Y. Yao, J. Hou and L. Sun, *Appl. Catal., B*, 2018, **227**, 54–60.

19 C. Yan, H. Li, Y. Ye, H. Wu, F. Cai, R. Si, J. Xiao, S. Miao, S. Xie, F. Yang, Y. Li, G. Wang and X. Bao, *Energy Environ. Sci.*, 2018, 1204–1210.

20 J. Tang and J. Wang, *Environ. Sci. Technol.*, 2018, **52**, 5367–5377.

21 H. Xu, J.-X. Feng, Y.-X. Tong and G.-R. Li, *ACS Catal.*, 2017, **7**, 986–991.

22 P. Wang, J. Wang, X. F. Wang, H. G. Yu and J. G. Yu, *Curr. Nanosci.*, 2015, **11**, 462–469.

23 H. Hu, Y. Tang, Q. Hu, P. Wan, L. Dai and X. J. Yang, *Appl. Surf. Sci.*, 2018, **445**, 281–286.

24 J. H. Montoya, C. Shi, K. Chan and J. K. Norskov, *J. Phys. Chem. Lett.*, 2015, **6**, 2032–2037.

25 E. Bertheussen, A. Verdaguer-Casadevall, D. Ravasio, J. H. Montoya, D. B. Trimarco, C. Roy, S. Meier, J. Wendland, J. K. Norskov, I. E. L. Stephens and I. Chorkendorff, *Angew. Chem., Int. Ed.*, 2016, **55**, 1450–1454.